processes

MDPI

Article

Effect of Automated Multi-Pass MAG Welding Parameters on the Fracture Toughness and Hydrogen Embrittlement Susceptibility of API 5L X70 Pipeline Steel

Danko Ćorić *, Kristijan Jurgec, Ivica Garašić and Maja Remenar

Faculty of Mechanical Engineering and Naval Architecture, University of Zagreb, Ivana Lučića 5, 10000 Zagreb, Croatia; kristijan.jurgec@fsb.unizg.hr (K.J.); ivica.garasic@fsb.unizg.hr (I.G.); maja.remenar@fsb.unizg.hr (M.R.)

* Correspondence: danko.coric@fsb.unizg.hr

Abstract

Welded joints in API 5L X70 pipeline steel represent critical locations for pipelines intended for hydrogen service because welding can create microstructural inhomogeneity, stress concentrations, and uneven mechanical properties that can promote hydrogen-assisted degradation. In hydrogen-containing environments, these effects may manifest as reduced ductility, loss of fracture resistance, and increased cracking susceptibility, particularly in the weld metal and heat-affected zone. Therefore, welding procedures for X70 intended for hydrogen applications must be evaluated using systematic mechanical testing and microstructural characterization under defined hydrogen exposure conditions. The study investigates the detrimental effects of hydrogen on the mechanical integrity of pipeline materials, focusing on welded joints of the API 5L X70 steel, a candidate material for use in hydrogen-containing environments. The weldability and structural performance of the X70 pipeline steel joints in hydrogen environments, produced using automated multi-pass metal active gas (MAG) welding, was experimentally studied. Welding was performed on a DN800 pipe with precise control over welding parameters. Comprehensive analyses were conducted on the welded joints, including microstructure examinations, hardness measurements, slow strain rate testing in high-pressure gaseous H_2 with a N_2 baseline and fracture toughness testing. In high-pressure hydrogen SSRT showed a moderate reduction in ductility relative to nitrogen, with reduction of area decreasing from 81.2% (N_2) to 69.1 and 71.5% (H_2), while time-to-failure remained comparable (475 min in N_2 vs. 497 and 496 min in H_2) Ultimate tensile strength was not reduced (579 MPa in N_2 vs. 609 and 597 MPa in H_2). Secondary surface cracks were observed only on specimens tested in hydrogen. Fracture mechanics testing after hydrogen exposure yielded K_{IH} values of 58–59 MPa$\sqrt{m}$ in the weld metal and 57–61 MPa$\sqrt{m}$ in the HAZ, exceeding the 55 MPa$\sqrt{m}$ acceptance threshold applied in this study. The results highlight the necessity of optimized welding techniques and targeted material analyses to ensure the safety and durability of pipelines in hydrogen-rich environments, thereby contributing to the development of reliable infrastructure for sustainable energy systems.

Keywords: hydrogen embrittlement; high-strength steel; automated MAG welding; pipeline welding; material testing

Check for updates

Academic Editor: Fábio Fernandes

Received: 20 February 2026
Revised: 19 March 2026
Accepted: 24 March 2026
Published: 27 March 2026

Copyright: © 2026 by the authors. Licensee MDPI, Basel, Switzerland. This article is an open access article distributed under the terms and conditions of the Creative Commons Attribution (CC BY) license.

1. Introduction

Hydrogen can appear in materials from various sources, including manufacturing processes and material processing. It also arises as a result of chemical reactions [1]. The presence of hydrogen in welding joints presents a serious problem as it can cause material degradation [2]. Its interactions with metallic structures significantly influence the relationship between microstructure and the properties of engineering alloys. Hydrogen in pipeline service can degrade the mechanical performance of welded joints by reducing ductility and facilitating crack initiation and growth. For API 5L X70 pipeline steel, welding is a key challenge for hydrogen environments because the thermal cycle creates a heterogeneous joint (weld metal and multiple HAZ subregions) with local microstructural gradients, potential hard zones, and residual stresses that can increase hydrogen sensitivity. As an HSLA steel, X70 derives strength from microalloying and a refined microstructure, which increases the density of interfaces and defects that can act as hydrogen traps. Combined with weld-induced heterogeneity and residual stresses, this can elevate hydrogen-assisted cracking susceptibility in local WM/HAZ regions. Consequently, hydrogen-related qualification of X70 welds must focus on WM and HAZ microstructures and their fracture/ductility response under defined hydrogen exposure conditions [3–6].

Hydrogen degradation is governed by environment/exposure, temperature/pressure, stress state, and microstructural sensitivity; damage typically occurs when sufficient hydrogen accumulates under stress in a susceptible microstructure [7]. Hydrogen can cause several damage manifestations in steel, including cracking and the appearance of pores. Some of the terminological terms related to the damage caused by the presence of hydrogen in the material include: hydrogen embrittlement (HE), stress corrosion cracking (SCC), stress-oriented hydrogen-induced cracking (SOHIC), stepwise cracking (SWC), and hydrogen-induced cracking (HIC) [8]. The term hydrogen embrittlement (HE) refers to various damaging effects hydrogen has on materials, including brittleness and other property changes [9]. Under static increasing load, the primary concern for X70 welds in hydrogen service include hydrogen-induced cracking and bubbling, whereas under cyclic loading a key integrity concern is hydrogen-assisted fatigue crack initiation and growth [10,11].

The hydrogen economy is a concept that represents the idea of transitioning from current energy systems, which are primarily based on fossil fuels, to systems where hydrogen is primarily used as an energy carrier, for energy storage, as well as a fuel [12]. The goal of the hydrogen economy is to reduce dependence on fossil fuels, decrease greenhouse gas emissions, and promote the sustainable use of renewable energy sources [13]. Transportation and storage of hydrogen are key elements of the hydrogen value chain, as hydrogen production often occurs at locations distant from the points of consumption. Hydrogen can be stored and transported in several forms, including compressed gaseous hydrogen, liquid hydrogen, and hydrogen in metal hydrides [14]. The transportation of compressed hydrogen through pipelines emerges as one of the most economical options for the continuous transport of large quantities of hydrogen from the production site to the end user. However, constructing new hydrogen pipelines can require substantial initial investments. Hydrogen transportation can also be achieved using the existing gas transport infrastructure by mixing hydrogen with natural gas and then separating it from the mixture where there is a need for pure hydrogen [15]. There are significant differences between various pipeline and equipment materials, and therefore it is necessary to conduct targeted evaluations on different pipelines. Further research is required into the synergetic effects of hydrogen with sulfur, carbon monoxide, and carbon dioxide on material. Generally, there is still a lack of research dealing with the prediction of damage and measures to minimize damage caused by the presence of hydrogen in materials used for constructing pipelines and other elements of the existing gas infrastructure [2].

In pipelines where a mixture of natural gas and hydrogen is present under elevated pressure, the likelihood of damage occurrence significantly increases. The main method for connecting segments of pipelines for transporting natural gas, and potentially hydrogen mixed with natural gas, is welding. Welding joints between the pipe segments represent critical areas, especially vulnerable to damage caused by hydrogen. The inhomogeneity of the weld microstructure, stress concentrations, and uneven mechanical properties within the weld can particularly compromise the structural integrity of structures in a hydrogen environment [16–18]. Understanding the degradation mechanisms and exploring strategies to enhance and maintain the mechanical properties of welded joints in high-pressure hydrogen environments has emerged as a critical area of research supporting the advancement of the hydrogen economy [19]. The lifespan of pipelines made from existing pipeline steels significantly reduces in the presence of hydrogen [18]. Welding introduces a large amount of energy in a short period of time, which can lead to unpredictable microstructures and residual stresses in the weld metal and its surroundings. Post-weld heat treatment can reduce welding-induced residual stresses, which may improve resistance to hydrogen-assisted cracking [20]. In hydrogen service conditions, the weld metal and heat-affected zone (HAZ) are particularly susceptible to hydrogen accumulation, which promotes embrittlement [2]. By properly selecting the welding processes and welding parameters, it is possible to reduce the prerequisites for creating areas within the material microstructure that are sensitive to the negative effects of hydrogen [21]. Automated metal active gas (MAG) welding remains integral to the fabrication of steel pipelines due to its capability for precise parameter control, high weld reproducibility, and consistent weld quality [22]. Recent studies on pipeline steels have demonstrated that hydrogen exposure can reduce ductility and fracture resistance in weld metal and areas of the heat-affected zone, as observed in slow strain rate tensile tests and fracture toughness tests [23,24]. Such findings highlight the importance of systematic mechanical testing since empirical evaluation remains essential for verifying weld performance and ensuring the integrity of pipeline steels under hydrogen service conditions. There is limited published work that combines automated multi-pass MAG welding of API 5L X70 pipe with hydrogen-related testing and welded joint microstructure/property characterization. Therefore, this study evaluates an automated multi-pass MAG procedure on a DN800 X70 pipe by: characterizing WM/HAZ microstructures, mapping hardness across the joint, and assessing hydrogen response using SSRT in high-pressure gas with an inert baseline and K_{IH} testing.

2. Materials and Methods

The investigated material was an API 5L X70 pipeline steel pipe with an outside diameter of 813 mm (DN800) and a wall thickness of 14.3 mm (chemical composition and mechanical properties are provided in Tables 1 and 2, respectively). X70 is a high-strength, low-alloy (HSLA) steel primarily developed for the manufacturing of pipelines used in the transportation of oil, natural gas, and water over long distances and under high pressures. It belongs to the API 5L specification issued by the American Petroleum Institute, which defines the requirements for line pipe steels used in the oil and gas industry.

The joint preparation consisted of a U-groove with a 10° bevel angle, a root face height of 1.6–2.0 mm, and a root gap of 0–1 mm. The circumferential weld was completed in eight passes (Figure 1).

Accurate joint preparation was essential to achieving weld integrity. Improper alignment or an excessive root gap could negatively affect the formation of the root pass, which in turn influences the quality of subsequent fill and cap passes. Since the root provides the foundation for the entire weld, any deficiencies at this stage may reduce the overall reliability of the joint.

Table 1. Chemical composition of X70 steel.

Element	C	Si	Mn	P	S	Ni	Cr	Cu	V
Weight (%)	0.054	0.266	1.53	0.011	0.0052	0.05	0.013	0.010	0.014
Element	**Ca**	**Al**	**Mo**	**Ti**	**Nb**	**Sn**	**As**	**N**	
Weight (%)	0.0015	0.019	0.209	0.015	0.039	0.017	0.012	0.0085	

Table 2. Mechanical properties of X70 steel.

Steel Grade	Yield Strength $R_{e0.5}$, MPa, min.	Ultimate Tensile Strength R_m, MPa, min.	Elongation A_f, %, min.
X70	485	570	Determined according to API 5L

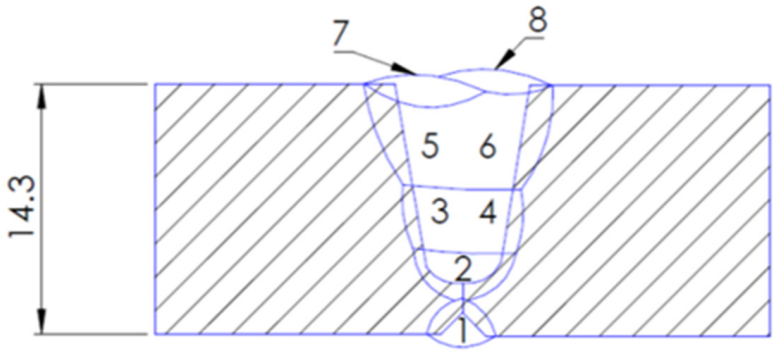


Figure 1. Welding sequence (numbers 1–8 represent designated welding passes).

Automated metal active gas (MAG) welding was used to ensure consistent heat input and reproducibility. Automated/mechanized MAG welding is widely used for pipeline fabrication because it improves process repeatability through consistent torch motion and tighter control of key parameters. This typically results in more consistent weld geometry and reduced operator-to-operator variability, and it can increase productivity through higher duty cycle and deposition efficiency. In addition, automated systems commonly enable parameter logging/traceability, which supports quality assurance for large-diameter pipeline construction where consistent thermal history is important when assessing hydrogen-related performance. The first two passes were deposited using spray transfer mode (135-S according to EN ISO 4063:2023 [25]), whereas subsequent passes were welded using pulsed transfer mode (135-P). Pipes were flame preheated to 100 °C, and welding of the subsequent passes was continued only when the interpass temperature dropped below 150 °C. The welding current decreased with the number of passes, with the root pass performed at 205 A. Detailed welding parameters are summarized in Table 3 and are based on preliminary trials and optimization.

Table 3. Welding parameters.

Pass No.	Welding Current, A	Voltage, V	Welding Speed, cm/min	Heat Input, kJ/mm
1	205	20.5	70.0	0.288
2	270	25.0	115.0	0.282
3–4	190	23.0	48.0	0.437
5–6	175	20.0	48.0	0.350
7–8	140	23.0	51.0	0.303

The shielding gas was a mixture of 80% Ar and 20% CO_2, designation M21 according to EN ISO 14175 [26]. The flow rate was in the range from 30 to 43 L/min. As a filler material, a Böhler solid wire conforming to the EN ISO 14341 [27] classification G 46 4 M21 4Si1 was employed (chemical composition is provided in Table 4). For welding of the root pass, a Ø 0.9 mm wire was used, whereas the remaining passes were welded using a Ø 1.0 mm filler wire.

Table 4. Chemical composition of filler material.

Element	C	Si	Mn	P	S
Weight (%)	0.069	0.95	1.65	≤0.02	≤0.015

For metallographic analysis, samples were sectioned and subjected to a conventional preparation sequence. Grinding was carried out using SiC abrasive papers with increasing grit sizes, followed by polishing using diamond pastes. The polished surfaces were etched with a 3% nital, a solution of nitric acid and alcohol, in order to reveal the weld zones. Macrostructural analysis was used to evaluate weld geometry and overall soundness, while microstructural examination was performed using an Olympus GX51 optical microscope (Olympus, Evident, Berlin, Germany).

Hardness testing was performed according to HRN EN ISO 9015-1:2012 [28] and using the Vickers method with a 10 kgf load (HV10). Measurements were made across three lines covering the upper weld, root, and lower weld zones.

In addition to metallographic and hardness measurements, mechanical testing was carried out to assess the behavior of the welded joint in hydrogen environments. Slow strain rate tests (SSRTs) were performed on specimens extracted from the weld region. Tests were conducted at a controlled displacement rate in a sealed high-pressure chamber at room temperature in 100 bar N_2 (inert baseline) and 100 bar H_2 to evaluate susceptibility to hydrogen-assisted cracking. The hydrogen gas was of high purity (Alphagaz 2, quality 6.0, 99.9999% H_2 min.), having the following limits on impurities: O_2 < 1 ppm, CO_2 < 1 ppm, CO < 1 ppm, H_2O < 3 ppm. During the test, the specimens were subjected to a constant displacement for 1000 h at room temperature. The threshold stress-intensity factor for hydrogen-assisted cracking (K_{IH}) was obtained under controlled loading conditions (according ASME BPVC Section VIII Division 3 KD-1043 K_{IH} testing procedures can be applied if the specimen thickness is above 85% of the wall thickness). These tests provided a quantitative measure of material crack resistance.

3. Results and Discussion

3.1. Metallographic Examination

Etching of the welded joint material revealed a sound circumferential weld with clearly visible regions of base metal (BM), heat-affected zone (HAZ), and weld metal (WM). An image of the sample is shown in Figure 2.

The HAZ exhibits uniform width across the joint, which indicates stable heat input and consistent welding parameters during welding. No macroscopic imperfections such as cracks, porosity, lack of fusion, or undercut were observed. The individual welding passes are distinguishable, and the final weld pass shows an even profile with consistent height and no visible surface defects. These observations confirm that the applied welding procedure ensured sound joint geometry and stable thermal cycles. For a more detailed characterization of phase composition and grain morphology, metallographic analysis was extended to the microstructural level.

The base material exhibits a fine-grained microstructure composed mainly of polygonal ferrite and acicular ferrite, with smaller fractions of pearlite, as seen in Figure 3.

The structure appeared homogeneous and free of inclusions, reflecting the controlled thermomechanical processing of the pipe material.

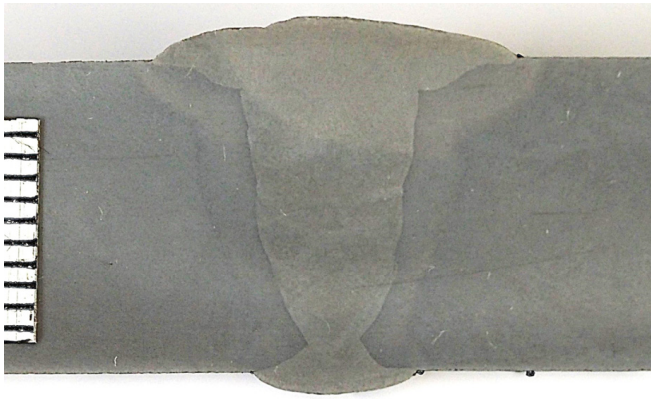


Figure 2. Macroscopic view of the sample.

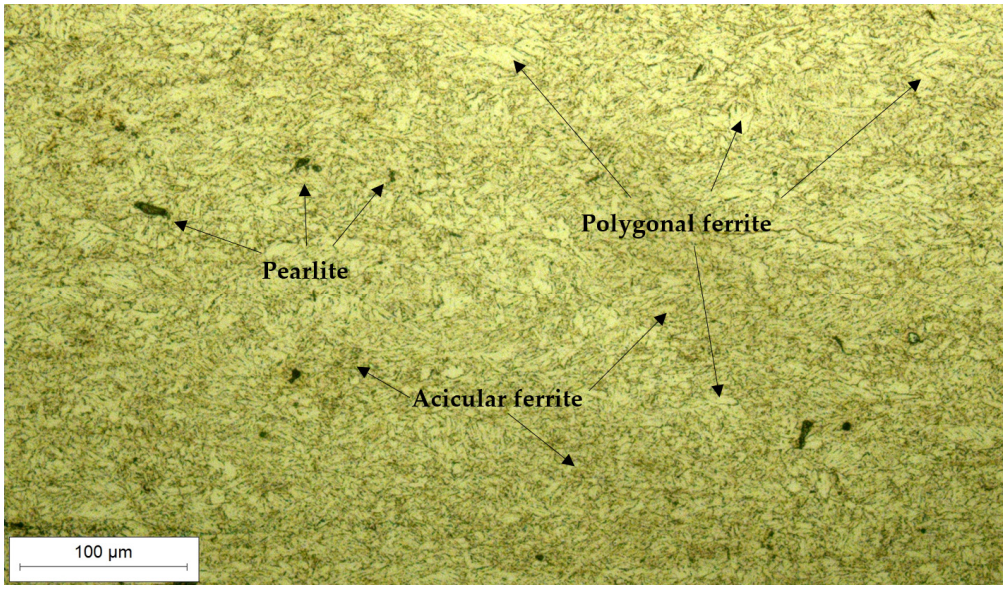


Figure 3. Microstructure of the base material.

The heat-affected zone shown in Figure 4 was found to contain a coarser microstructure compared to the base material, dominated by acicular ferrite and bainite. The entire transition from weld metal to the base material through different HAZs is shown in Figure 5. The area of the ICHAZ was exposed to peak temperatures between the A_1 and A_3 transformation boundaries. Under these conditions, only a fraction of the base microstructure was austenitized. Upon cooling, the partially austenitized regions transformed predominantly into martensite–austenite (M–A) constituents, fresh martensite, or upper bainite, depending on the local cooling rate. Consequently, the ICHAZ exhibits a heterogeneous mixture of tempered ferrite, tempered bainite, and discrete M–A islands, a morphology that may promote local softening or embrittlement in X70 steels. The FGHAZ, on the other hand, experienced peak temperatures slightly above the A_3 temperature, causing full austenitization while maintaining a relatively fine austenite grain size. During cooling, this region transformed into fine bainite, acicular ferrite, and limited amounts of polygonal ferrite.

Grain boundaries are more pronounced, and grain size increases progressively closer to the fusion line. This variation is attributed to the steep thermal gradients and different peak temperatures experienced during welding. Closer to the BM, finer ferrite morphologies were typically retained, whereas regions closer to the WM evolved into coarser bainitic

structures. The heterogeneity of the HAZ is of particular importance for hydrogen service, as coarse-grained and bainitic morphologies have been shown to exhibit higher sensitivity to hydrogen-assisted cracking compared to finer ferritic structures [23,29].

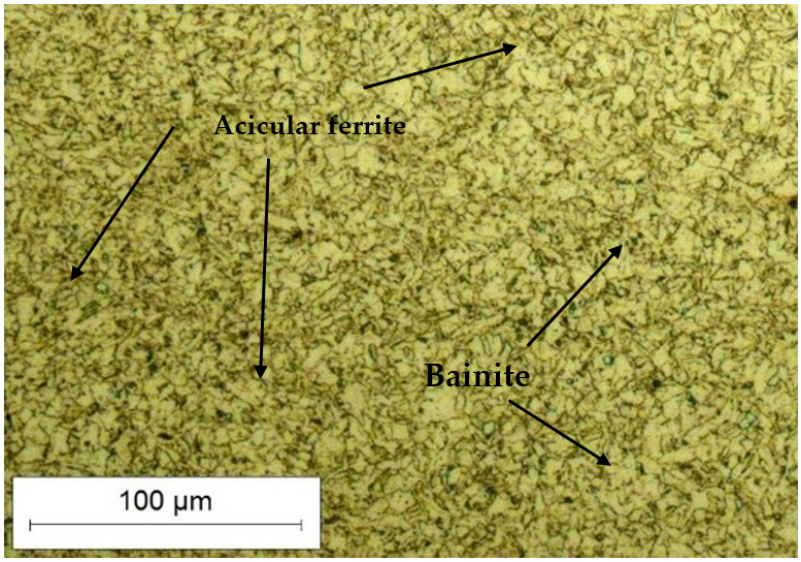


Figure 4. Microstructure of HAZ (FGHAZ).

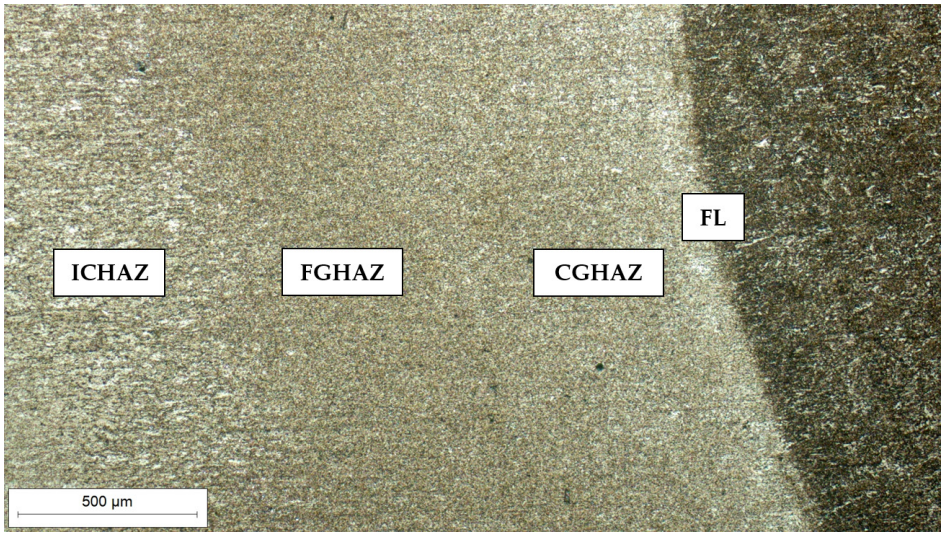


Figure 5. Transition area from weld metal, fusion line and through all HAZs.

At the fusion boundary (Figure 6), the microstructure consists of a combination of bainite, acicular ferrite, and localized polygonal ferrite. This narrow zone marks the interface between the HAZ and the WM. Columnar grains that developed in the WM extend toward the fusion line, oriented approximately perpendicular to it, reflecting the direction of heat extraction during solidification.

The alignment of these columnar grains may provide preferential paths for crack propagation under hydrogen-assisted conditions, making the fusion boundary a critical region for welded joint integrity [30].

The weld metal is predominantly composed of acicular ferrite, with polygonal ferrite also present. Local variations were observed within the weld metal, where a fine-grained ferritic structure containing bainite, polygonal ferrite, and acicular ferrite transformed into coarser polygonal ferrite (Figure 7).

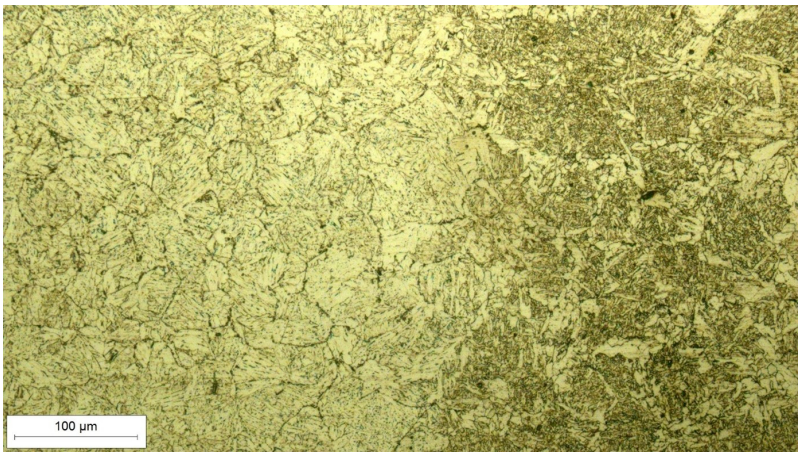
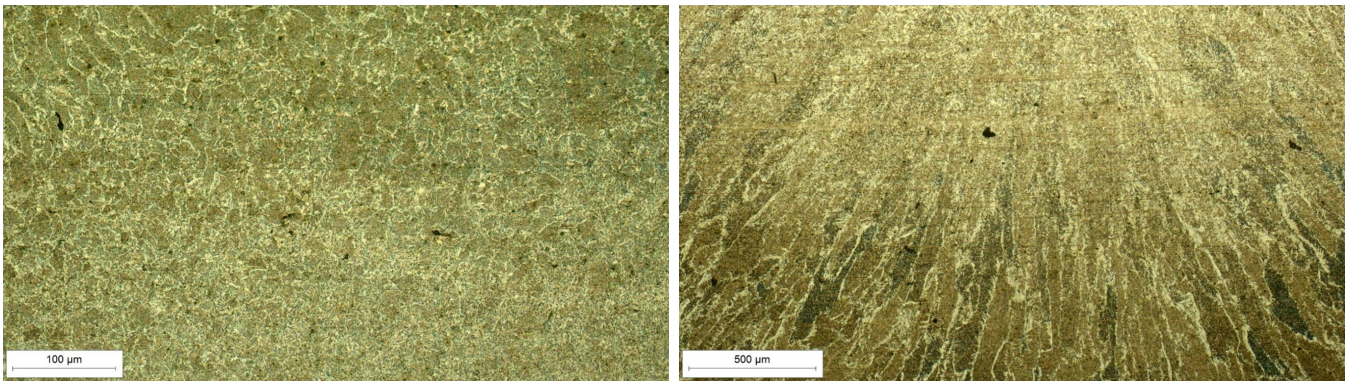


Figure 6. Fusion line microstructure.



(**a**) (**b**)

Figure 7. Microstructure of the weld metal: (**a**) near the weld face; (**b**) microstructure of the weld metal.

Overall, the WM exhibited the most uniform grain size and the most homogeneous microstructure compared to other zones of the joint. The presence of acicular ferrite is generally associated with improved toughness and partial resistance to crack propagation, although hydrogen-assisted degradation can still occur due to the combined effects of inclusions and hard secondary phases [31].

3.2. Hardness Measurements

Vickers hardness testing (HV10) was performed across the welded joint to evaluate the variation in hardness between the base metal, heat-affected zone and weld metal. The layout of indentation lines and measurement locations is shown in Figure 8.

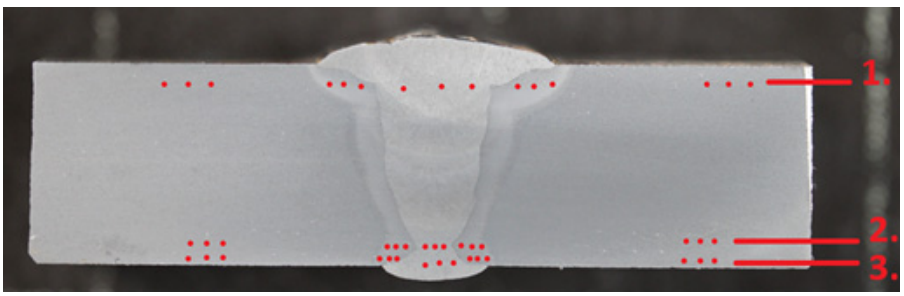


Figure 8. Hardness measurement locations (numbers 1, 2 and 3 denote measurements taken in the areas: face of the weld, root of the weld and back side of the weld respectively).

The hardness profiles along all three measurement lines were uniform, with no abrupt changes across the weld zones. The hardness values measured along three horizontal lines across the welded joint are shown in Table 5.

Table 5. Measured hardness values.

Series/Weld Zone	BM	HAZ	WM	HAZ	BM
1	180	169	173	209	165
	170	175	171	155	162
	171	228	175	164	163
2	178	163	178	225	213
	170	160	218	206	221
	162	167	228	212	220
3	224	162	221	230	224
	209	178	222	221	230
	209	228	227	215	232

The overall average hardness values were approximately 195 HV in the BM, 193 HV in the HAZ, and 201 HV in the WM, resulting in an overall mean hardness of about 195 HV. Heat input and cooling rate strongly influence WM/HAZ transformation behavior, local hardness, and the residual stress. Higher heat input and the applied pre-heat/interpass temperature control reduce cooling-rate severity and can reduce the likelihood of formation of high-hardness regions that are typically more susceptible to hydrogen-assisted cracking. In multi-pass welding, reheating by subsequent passes can further temper previously transformed regions and modify local defect structures and interfaces that act as hydrogen trapping sites. The small variation in average hardness value, within 4–5% across the joint, indicates balanced distribution and confirms that the applied welding parameters ensured stable heat input.

Although the elevated Mn and Mo contents (Table 1) could promote creation of local hard zones, the measured hardness profile shows no localized hardness peaks in the HAZ or WM, indicating that the selected welding procedure mitigated this risk. This observation is consistent with the metallographic results (Section 3.1), which showed the predominance of acicular ferrite in the WM and controlled grain coarsening in the HAZ. Such a uniform hardness profile across the weld cross-section is desirable for hydrogen service applications, as it minimizes the likelihood of hydrogen-assisted cracking initiation.

3.3. Stress Corrosion Susceptibility

Slow strain rate testing (SSRT) was carried out on cylindrical specimens extracted from the weld metal in accordance with DIN EN ISO 7539-7:2018 [32] to assess susceptibility to hydrogen-assisted cracking. The tests were performed at room temperature and a strain rate of 1×10^{-5} s^{-1}. The specimens had a gauge length of 25.4 mm and a diameter of 6.35 mm. The tensile axis was perpendicular to the weld seam (transverse orientation). This ensured that the applied load acted across all weld regions. Two gaseous environments were applied:

- Nitrogen at 100 bar, serving as the inert reference condition.
- Hydrogen at 100 bar, representing the service environment.

The susceptibility of steel to stress corrosion cracking (SCC) was evaluated by comparing its mechanical properties measured in a specific corrosive medium with those obtained in a controlled environment, namely nitrogen. For all slow strain rate tests (SSRTs), variations in the time to failure ratio (*TTFR*), reduction in area ratio (*RAR*), and plastic elongation ratio (E_pR) were determined. SCC susceptibility was expressed in terms of the percent-

age reduction in area (%RA), calculated according to the NACE TM-0198 [33] using the following equation:

$$\%RA = \frac{\left(D_i^2 - D_f^2\right)}{D_i^2} \quad (1)$$

where D_i and D_f are the initial and final diameters of the tensile specimen, respectively. The reduction in area ratio (RAR) was calculated as the ratio between the reduction in area after fracture measured in the test environment (RA_e) and the corresponding value obtained in the controlled environment (RA_c), as shown in Equation (2):

$$RAR = \frac{RA_e}{RA_c} \quad (2)$$

In addition, the time to failure ratio ($TTFR$) was evaluated as an additional parameter for comparing SCC susceptibility, according to Equation (3):

$$TTFR = \frac{TTF_e}{TTF_c} \quad (3)$$

where TTF_e is the time to failure measured in the test environment and TTF_c is the time to failure measured in the controlled environment (nitrogen). Similarly, the plastic elongation ratio (E_pR) was calculated using Equation (4):

$$E_pR = \frac{E_{pe}}{E_{pc}} \quad (4)$$

where E_{pe} is the plastic elongation to failure in the test environment (%), E_{pc} is the plastic elongation to failure in the controlled environment (%).

The test results are summarized in Tables 6 and 7 and Figure 9 shows the SSRT curves obtained by the test.

Table 6. Summary of SSRT results for specimens tested in nitrogen and hydrogen atmosphere.

Specimen	Environment	*RA*, %	E_{tot}, %	E_p, %	*TTF*, min	*UTS*, MPa	Secondary Cracks
01	N_2 (100 bar)	81.2	28.1	20.7	475	579	No
02	H_2 (100 bar)	69.1	29.3	19.5	497	609	Yes
03	H_2 (100 bar)	71.5	28.1	18.2	476	597	Yes

Table 7. SSRT ratio results for specimens tested in hydrogen atmosphere.

Specimen	Environment	*RAR*, %	$E_{tot}R$, %	E_pR, %	*TTFR*, %	*UTSR*, %
02	H_2 (100 bar)	85.1	104.3	94.2	104.6	105.2
03	H_2 (100 bar)	88.1	100.0	87.9	100.2	103.1

The total strain to failure remained almost unchanged in hydrogen compared with nitrogen, while the reduction of area (RA) decreased up to almost 15% in the hydrogen environment. This indicates that hydrogen did not strongly influence deformation along the length but reduced the ability of the material to sustain localized plastic deformation during necking. The ultimate tensile strength (UTS) was essentially unaffected, remaining between 579 and 609 MPa in both environments. The SCC index values of $TTFR$, RAR, $E_{tot}R$ and E_pR from 0.8 to 1 indicate that the material has good resistance to SCC and values lower than 0.8 indicate that the material could be susceptible to SCC [34]. Analyzing the SCC

index values of measured properties shown in Table 7, it can be seen that all values are well over 0.8 (80%) with some values indicating even better properties in the test environment (hydrogen) and very good resistance of the welded joint to SCC.

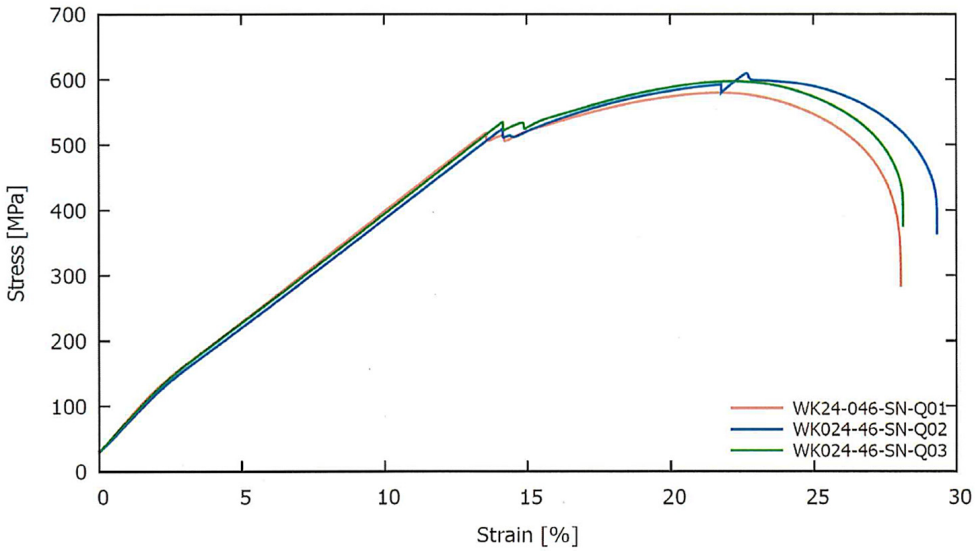


Figure 9. SSRT curves for all the samples.

The ductility reduction and secondary cracking during the SSRT in hydrogen can be discussed in terms of hydrogen's interaction with microstructural features. In HSLA weldments, hydrogen can be trapped at microstructural defects and interfaces such as dislocations, grain boundaries, inclusions and phase boundaries. These sites can promote localized damage under stress. The WM/HAZ heterogeneity provides a range of interfaces that may act as preferential sites for hydrogen-assisted crack initiation, consistent with the appearance of secondary cracking in hydrogen [35,36].

Although the global mechanical properties appear similar, the formation of secondary surface cracks on the specimens tested in hydrogen suggests the occurrence of local hydrogen-assisted damage mechanisms. These microcracks typically initiate at stress concentrators, such as inclusions or grain-boundary interfaces, where hydrogen accumulates, promoting localized decohesion or quasi-cleavage fractures. Such phenomena can occur even when properties like elongation or strength show minimal overall change. The combination of nearly constant elongation and reduced reduction of area therefore indicates that hydrogen mainly affects the fracture localization behavior rather than the general plastic flow of the weld metal. The welded joint thus demonstrates limited but measurable susceptibility to hydrogen-induced damage under the applied test conditions. A similar response has been reported by Shuai et al. [37], who found that, in X70 pipeline steel welds exposed to high-pressure hydrogen, overall tensile strength remained unchanged while microcracking and localized embrittlement developed on the fracture surface, leading to a transition from fully ductile to mixed ductile + quasi-cleavage fracture modes. These observations are consistent with the moderate hydrogen sensitivity found in this study, confirming that the mechanical integrity of the weld metal is largely preserved but that localized damage processes may still occur.

3.4. Fracture Toughness Evaluation

Fracture toughness testing was conducted to evaluate the resistance of the welded joint to hydrogen-assisted cracking. Specimens were machined from both the weld metal and the heat-affected zone. Testing followed the procedures specified in ASTM E1681-2013 [38] and ASME BPVC Section VIII, Division 3 (2013) [39], which define qualification requirements

for steels used in high-pressure hydrogen service. The thickness of the machined specimens was set to at least 85% of the design thickness of the pipe material that was qualified. The test specimen drawing including important dimensions (specimen thickness (B), specimen width (W), and fatigue crack size (a)) is given in Figure 10. Prior to testing, all specimens were exposed to pure hydrogen gas at 100 bar and room temperature for 1000 h to ensure adequate hydrogen charging. Diffusible hydrogen content was not measured in this study. Accordingly, results are interpreted as performance under the defined hydrogen exposure conditions rather than correlated to a measured hydrogen concentration. Fatigue pre-cracking was conducted in an ambient air environment with the specimen fully heat treated to the condition in which it was to be tested. The fatigue pre-crack extended to a depth of not less than 1.25 mm beyond the tip of the machined notch as measured on each face of the specimen. The final 1 mm increment of fatigue pre-cracking was conducted at a maximum stress-intensity factor (K_{max}) of not more than 60% of the expected K_{IH} value.

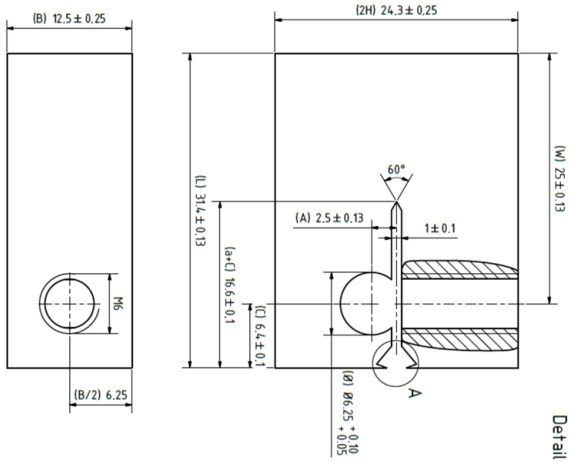


Figure 10. K_{IH} specimen geometry (B = 12.5) used for testing.

After the test, the specimens were unloaded and hydrogen-assisted cracking (HAC) advance marked by heat tinting the specimen at about 300 °C for 30 min. Crack growth was determined using a scanning electron microscope. Measurements were taken perpendicular to the pre-crack at 25% B, 50% B, and 75% B locations. The average of these three values was used for calculation of the K_{IH} value. Additionally, 3D images were obtained using light optical microscopy (Figure 11). A typical fracture surface of the specimen is shown in Figure 12. If the average measured crack growth exceeds 0.25 mm, K_{IH} shall be established with subcritical crack growth based on the final crack size a. The a/W ratio shall not exceed 0.95 ($a/W \leq 0.95$). The expression for K_{IAPP} given in Equation (5) is valid for H/W = 0.486 and for a/W from 0.3 to 0.95.

$$K_{IAPP} = \left[\frac{EV_m}{\sqrt{W}}\right] f\left(\frac{a}{W}\right) \quad (5)$$

with

$$f\left(\frac{a}{W}\right) = \left[\sqrt{1-\frac{a}{W}}\right]\left[0.654 - 1.88\left(\frac{a}{W}\right) + 2.66\left(\frac{a}{W}\right)^2 - 1.233\left(\frac{a}{W}\right)^3\right] \quad (6)$$

where:

V_m = crack-mouth opening displacement on the specimen face in mm,
E = Young's modulus in MPa (206,000 MPa),
a = final crack size in mm,
B = specimen thickness in mm, and
W = specimen width in mm.

If the average measured crack growth does not exceed 0.25 mm, K_{IH} is equal to 50% of K_{IAPP} (Equation (7)). Otherwise K_{IH} equals K_{IAPP}.

$$K_{IH} = \frac{K_{IAPP}}{2} \tag{7}$$

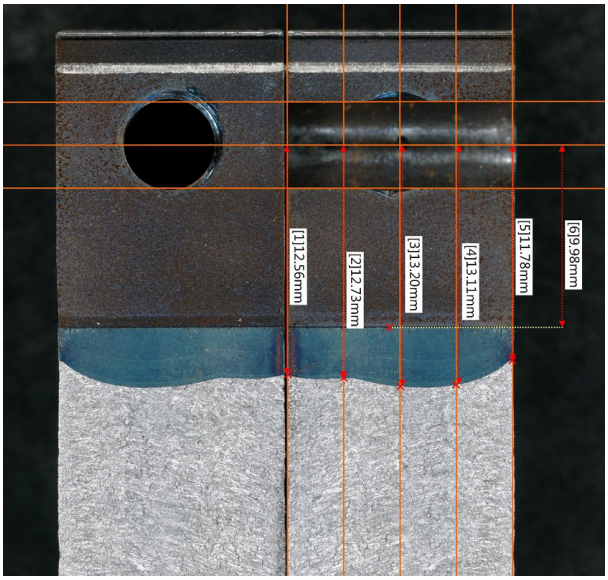


Figure 11. 3D optical microscopy image of the specimen.

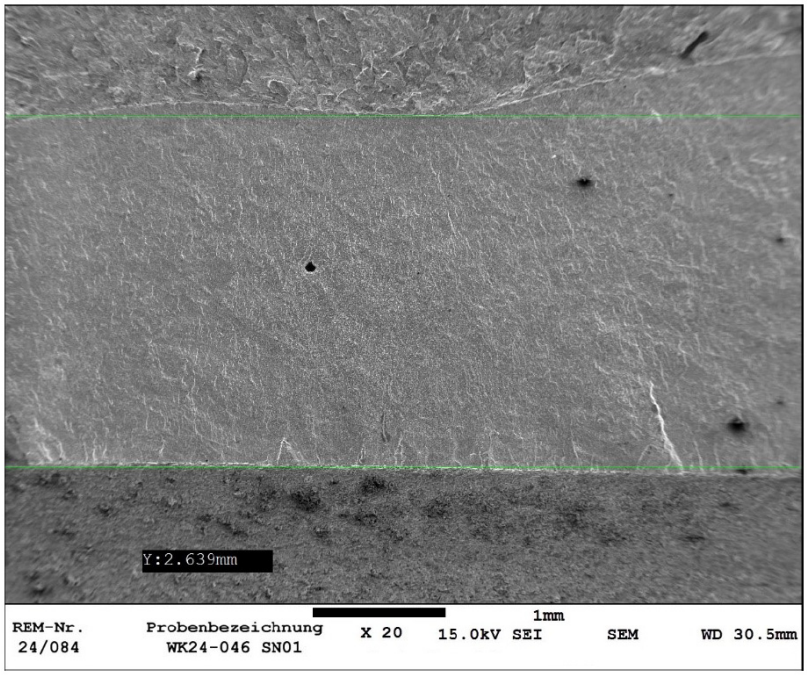


Figure 12. Typical fracture surface of a K_{IH} specimen without hydrogen crack growth; specimen WM1, measurement done at 25% wall thickness B (green lines represent reference lines).

The critical stress-intensity factor in hydrogen, K_{IH}, was then determined under controlled loading. For both the WM and HAZ, K_{IH} values were in the range of 57–61 MPa$\sqrt{\text{m}}$, exceeding the acceptance threshold according to ASTM E1681-2013 of 55 MPa$\sqrt{\text{m}}$ required for steels in hydrogen service (Table 8).

Table 8. K_{IH} values of the tested materials in accordance with ASTM E1681-2013 and ASME BPVC Section VIII Div 3—2013.

Sample Location	Specimen ID	$CMOD_i$	Crack Length *a*	K_{IH}	K_{IAPP}	K_{IH}, Min	K_{IH}, Avg
		mm	mm	MPa$\sqrt{m}$	MPa$\sqrt{m}$	MPa$\sqrt{m}$	MPa$\sqrt{m}$
WM	WM1	0.580	12.912	59	117		
WM	WM2	0.564	12.598	58	116	58	58
WM	WM3	0.559	12.478	58	116		
HAZ	HAZ1	0.553	12.038	59	118		
HAZ	HAZ2	0.557	12.581	57	115	57	59
HAZ	HAZ3	0.561	11.683	61	123		

These results confirm that the welded joint provides adequate resistance to hydrogen-assisted cracking. The close similarity of K_{IH} values in the WM and HAZ indicates that the applied MAG welding parameters produced a balanced microstructure and prevented formation of local brittle regions. The importance of assessing fracture toughness behavior in welded regions is well established, since hydrogen embrittlement susceptibility depends strongly on local microstructure and residual stresses across the joint [40]. The comparable K_{IH} levels measured for the WM and HAZ therefore indicate that the applied welding parameters produced a sufficiently uniform microstructure to maintain resistance to hydrogen-assisted cracking. The present results confirm that the tested MAG welded X70 joint retains sufficient fracture resistance for potential hydrogen pipeline applications.

4. Conclusions

The present study investigated the microstructural characteristics and mechanical performance of welded joints of API 5L X70 steel produced by automated MAG welding for potential use in hydrogen environments. Based on the results obtained, the following conclusions can be drawn:

1. The applied MAG welding procedure produced a sound circumferential joint without macrodefects, characterized by a stable weld geometry and uniform heat-affected zone width, confirming adequate control of welding parameters.
2. Microstructural analysis revealed that the weld metal consists mainly of acicular ferrite with portions of polygonal ferrite and bainite, while the HAZ contains a ferritic–bainitic structure with moderate grain coarsening toward the fusion line.
3. Hardness measurements showed a uniform distribution across the joint and no significant hardness peaks in different zones of the weld. The consistent hardness profile indicates a homogeneous microstructure and stable heat input during welding, minimizing the risk of brittle microstructural constituents.
4. Slow strain rate testing confirmed limited hydrogen sensitivity of the weld metal. Total elongation remained nearly unchanged in hydrogen compared to nitrogen, whereas the reduction of area decreased moderately, accompanied by isolated secondary cracking. These results suggest that hydrogen primarily influences local fracture processes rather than the overall deformation behavior of the joint.
5. Fracture toughness testing after exposure to 100 bar H_2 demonstrated that both the WM and HAZ maintain threshold stress-intensity factors between 57 and 61 MPa$\sqrt{m}$, exceeding the 55 MPa$\sqrt{m}$ acceptance limit for steels in hydrogen service. The similar K_{IH} levels for both regions confirm that the applied welding parameters yielded a balanced microstructure with no localized embrittlement.

6. Overall, the results show that automated MAG welding of API 5L X70 steel provides welded joints with sufficient structural integrity, uniform microstructure, and fracture resistance under high-pressure hydrogen exposure. These findings confirm the suitability of the applied welding procedure for hydrogen transport and storage components, while emphasizing the need for further studies under long-term cyclic and variable-pressure conditions to evaluate service durability.

Author Contributions: Conceptualization, D.Ć. and I.G.; methodology, I.G., K.J. and M.R.; validation, D.Ć., I.G. and M.R.; formal analysis, M.R.; investigation, M.R. and I.G.; resources, I.G.; data curation, M.R.; writing—original draft preparation, K.J.; writing—review and editing, M.R., I.G. and K.J.; visualization, M.R. and K.J.; supervision, I.G. and D.Ć. All authors have read and agreed to the published version of the manuscript.

Funding: This paper has been funded by the European Union (NextGenerationEU) under the National Recovery and Resilience Plan 2021–2026 (NRRP), through the UNIZAG FSB institutional project "An integral approach to the strategy of data structuring for the application of artificial intelligence in the production and exploitation of welded structures", approved by the Ministry of Science, Education and Youth of the Republic of Croatia (component C3.2, source 581).

Data Availability Statement: The original contributions presented in the study are included in the article, further inquiries can be directed to the corresponding author.

Conflicts of Interest: The authors declare no conflicts of interest. The funders had no role in the design of the study; in the collection, analyses, or interpretation of data; in the writing of the manuscript; or in the decision to publish the results.

Abbreviations

The following abbreviations are used in this manuscript:

API	American Petroleum Institute
ASME	American Society of Mechanical Engineers
ASTM	American Society for Testing and Materials
BM	Base Material
BPVC	Boiler and Pressure Vessel Code
CMOD	Crack-Mouth Opening Displacement
DN	Nominal Diameter
EN	European Norm
E_pR	Plastic Elongation Ratio
HAZ	Heat-Affected Zone
FGHAZ	Fine-Grained Heat-Affected Zone
HE	Hydrogen Embrittlement
HIC	Hydrogen-Induced Cracking
HSLA	High-Strength Low-Alloy
H_2	Hydrogen
HV	Vickers Hardness
ICHAZ	Intercritical Heat-Affected Zone
ISO	International Organization for Standardization
K_{IH}	Threshold Stress-Intensity Factor for Hydrogen-Assisted Cracking
MAG	Metal Active Gas
NACE	National Association of Corrosion Engineers
N_2	Nitrogen
RA	Reduction of Area
RAR	Reduction in Area Ratio
SCC	Stress Corrosion Cracking

SiC	Silicon Carbide
SOHIC	Stress-Oriented Hydrogen-Induced Cracking
SSRT	Slow Strain Rate Test
SWC	Stepwise Cracking
TTFR	Time to Failure Ratio
UTS	Ultimate Tensile Strength
WM	Weld Metal
X70	API 5L Grade X70 Pipeline Steel

References

1. Li, W.; Cao, R.; Xu, L.; Qiao, L. The role of hydrogen in the corrosion and cracking of steels—A review. *Corros. Commun.* **2021**, *4*, 23–32. [CrossRef]
2. Ban, J.; Yan, X.; Song, B.; Deng, S.; Wu, H.; Tang, Y.; Yin, W. Research Progress and Prospects on Hydrogen Damage in Welds of Hydrogen-Blended Natural Gas Pipelines. *Processes* **2023**, *11*, 3180. [CrossRef]
3. Zhang, S.; Fan, E.; Wan, J.; Liu, J.; Huang, Y.; Li, X. Effect of Nb on the hydrogen-induced cracking of high-strength low-alloy steel. *Corros. Sci.* **2018**, *139*, 83–96. [CrossRef]
4. Breen, A.J.; Stephenson, L.T.; Sun, B.; Li, Y.; Kasian, O.; Raabe, D.; Herbig, M.; Gault, B. Solute hydrogen and deuterium observed at the near atomic scale in high-strength steel. *Acta Mater.* **2020**, *188*, 108–120. [CrossRef]
5. Alvaro, A.; Olden, V.; Macadre, A. Hydrogen embrittlement susceptibility of a weld simulated X70 heat affected zone under H_2 pressure. *Mater. Sci. Eng. A* **2014**, *597*, 29–36. [CrossRef]
6. Singh, R.; Singh, V.; Arora, A.; Mahajan, D.K. In-situ investigations of hydrogen influenced crack initiation and propagation under tensile and low cycle fatigue loadings in RPV steel. *J. Nucl. Mater.* **2020**, *529*, 151912. [CrossRef]
7. Hoschke, J.; Chowdhury, M.F.W.; Venezuela, J.; Atrens, A. A review of hydrogen embrittlement in gas transmission pipeline steels. *Corros. Rev.* **2023**, *41*, 277–317. [CrossRef]
8. Martin, M.L.; Sofronis, P. Hydrogen-induced cracking and blistering in steels: A review. *J. Nat. Gas Sci. Eng.* **2022**, *101*, 104547. [CrossRef]
9. Li, X.; Ma, X.; Zhang, J.; Akiyama, E.; Wang, Y.; Song, X. Review of Hydrogen Embrittlement in Metals: Hydrogen Diffusion, Hydrogen Characterization, Hydrogen Embrittlement Mechanism and Prevention. *Acta Metall. Sin. (Engl. Lett.)* **2020**, *33*, 759–773. [CrossRef]
10. Zhang, H.; Zhao, J.; Li, J.; Yu, B.; Wang, J.; Lyu, R.; Xi, Q. Research progress on corrosion and hydrogen embrittlement in hydrogen–natural gas pipeline transportation. *Nat. Gas Ind. B* **2023**, *10*, 570–582. [CrossRef]
11. Nanninga, N.; Slifka, A.; Levy, Y.; White, C. A review of fatigue crack growth for pipeline steels exposed to hydrogen. *J. Res. Natl. Inst. Stand. Technol.* **2010**, *115*, 437–452. [CrossRef]
12. Yap, J.; McLellan, B. A Historical Analysis of Hydrogen Economy Research, Development, and Expectations, 1972 to 2020. *Environments* **2023**, *10*, 11. [CrossRef]
13. Rissman, J.; Bataille, C.; Masanet, E.; Aden, N.; Morrow, W.R.; Zhou, N.; Elliott, N.; Dell, R.; Heeren, N.; Huckestein, B.; et al. Technologies and policies to decarbonize global industry: Review and assessment of mitigation drivers through 2070. *Appl. Energy* **2020**, *266*, 114848. [CrossRef]
14. Hren, R.; Vujanović, A.; Van Fan, Y.; Klemeš, J.J.; Krajnc, D.; Čuček, L. Hydrogen production, storage and transport for renewable energy and chemicals: An environmental footprint assessment. *Renew. Sustain. Energy Rev.* **2023**, *173*, 113113. [CrossRef]
15. Zhang, C.; Shao, Y.; Shen, W.; Li, H.; Nan, Z.; Dong, M.; Bian, J.; Cao, X. Key Technologies of Pure Hydrogen and Hydrogen-Mixed Natural Gas Pipeline Transportation. *ACS Omega* **2023**, *8*, 19212–19222. [CrossRef]
16. Sun, Y.; Cheng, Y.F. Hydrogen-induced degradation of high-strength steel pipeline welds: A critical review. *Eng. Fail. Anal.* **2022**, *133*, 105985. [CrossRef]
17. Zhao, W.; Yang, M.; Zhang, T.; Deng, Q.; Jiang, W.; Jiang, W. Study on hydrogen enrichment in X80 steel spiral welded pipe. *Corros. Sci.* **2018**, *133*, 251–260. [CrossRef]
18. Zhuo, J.; Zhang, C.; Zhang, S.; Chen, L.; Yang, H.; Liu, F.; Du, Y.; Lv, L.; Zheng, S. Influence of hydrogen environment on fatigue fracture morphology of X80 pipeline steel. *J. Mater. Res. Technol.* **2023**, *22*, 1039–1047. [CrossRef]
19. Su, Y.; Li, J.; Yu, B.; Zhao, Y.; Han, D.; Sun, D. Modeling of Hydrogen Blending on the Leakage and Diffusion of Urban Buried Hydrogen-Enriched Natural Gas Pipeline. *Comput. Model. Eng. Sci.* **2023**, *136*, 1315–1337. [CrossRef]
20. Chiocca, A.; Frendo, F.; Aiello, F.; Bertini, L. Influence of residual stresses on the fatigue life of welded joints. Numerical simulation and experimental tests. *Int. J. Fatigue* **2022**, *162*, 106901. [CrossRef]

21. Poznyakov, V.D.; Markashova, L.I.; Shelyagin, V.D.; Zhdanov, S.L.; Bernats'kYi, A.V.; Berdnikova, O.M.; Sydorets', V.M. Cold Cracking Resistance of Butt Joints in High-Strength Steels with Different Welding Techniques. *Strength Mater.* **2019**, *51*, 843–851. [CrossRef]
22. Park, J.H.; Moon, H.S. Advanced Automatic Welding System for Offshore Pipeline System with Seam Tracking Function. *Appl. Sci.* **2020**, *10*, 324. [CrossRef]
23. Tang, L.; Liu, W.; Gao, B.-C.; Sha, J.-T.; Bai, R.-X.; Che, B.-H.; Xu, K.; Qiao, G.-Y.; Xiao, F.-R. Study on Hydrogen Embrittlement Behavior in Heat-Affected Zone of X80 Welded Pipe. *Metals* **2025**, *15*, 414. [CrossRef]
24. Moser, N.; Buck, Z.; Derimow, N.; Martin, M.L.; Lauria, D.; Lucon, E.; Bradley, P.; Connolly, M. Hydrogen embrittlement susceptibility and fracture toughness measurements of welded X65M pipeline steels. In *Proceedings of the ASME 2024 Pressure Vessels & Piping Conference, Bellevue, WA, USA, 28 July–2 August 2024*; American Society of Mechanical Engineers, Pressure Vessels and Piping Division (Publication) PVP: Anaheim, CA, USA, 2024; Volume 4. [CrossRef]
25. *ISO 4063:2023*; Welding, Brazing, Soldering and Cutting—Nomenclature of Processes and Reference Numbers. ISO Switzerland: Geneva, Switzerland, 2023.
26. *EN ISO 14175:2008*; Welding Consumables—Gases and Gas Mixtures for Fusion Welding and Allied Processes. ISO Switzerland: Geneva, Switzerland, 2008.
27. *EN ISO 14341:2020*; Welding Consumables—Wire Electrodes and Weld Deposits for Gas Shielded Metal Arc Welding of Non Alloy and Fine Grain Steels—Classification. ISO Switzerland: Geneva, Switzerland, 2020.
28. *EN ISO 9015-1:2012*; Destructive Tests on Welds in Metallic Materials—Hardness testing—Part 1: Hardness Test on Arc Welded Joints. HZN Croatia: Zagreb, Croatia, 2012.
29. Qu, J.; Feng, M.; An, T.; Bi, Z.; Du, J.; Yang, F.; Zheng, S. Hydrogen-Assisted Crack Growth in the Heat-Affected Zone of X80 Steels during in Situ Hydrogen Charging. *Materials* **2019**, *12*, 2575. [CrossRef]
30. Mohtadi-Bonab, M.A.; Ariza-Echeverri, E.A.; Masoumi, M.A. Comparative Investigation of the Effect of Microstructure and Crystallographic Data on Stress-Oriented Hydrogen Induced Cracking Susceptibility of API 5L X70 Pipeline Steel. *Metals* **2022**, *12*, 414. [CrossRef]
31. Zhang, P.; Laleh, M.; Hughes, A.E.; Marceau, R.K.W.; Hilditch, T.; Tan, M.Y. Effect of microstructure on hydrogen embrittlement and hydrogen-induced cracking behaviour of a high-strength pipeline steel weldment. *Corros. Sci.* **2024**, *227*, 111764. [CrossRef]
32. *DIN EN ISO 7539-7:2018*; Corrosion of metals and alloys—Stress corrosion testing—Part 7: Method for slow strain rate testing. DIN Germany: Berlin, Germany, 2018.
33. *NACE TM0198-2020*; Slow Strain Rate Test Method for Screening Corrosion-Resistant Alloys for Stress Corrosion Cracking in Sour Oilfield Service. NACE USA: New York, NY, USA, 2020.
34. Galván-Martínez, R.; Carmona, A.; Baltazar, M.; Contreras, A.; Orozco-Cruz, R. Stress Corrosion Cracking of X70 Pipeline Steel immersed in Synthetic Soil solution. *Afinidad* **2019**, *76*, 52–62.
35. Chen, Y.S.; Huang, C.; Liu, P.-Y.; Yen, H.-W.; Niu, R.; Burr, P.; Moore, K.L.; Martínez-Pañeda, E.; Atrens, A.; Cairney, J.M. Hydrogen trapping and embrittlement in metals—A review. *Int. J. Hydrogen Energy* **2025**, *136*, 789–821. [CrossRef]
36. Barrera, O.; Bombac, D.; Chen, Y.; Daff, T.D.; Galindo-Nava, E.; Gong, P.; Haley, D.; Horton, R.; Katzarov, I.; Kermode, J.R.; et al. Understanding and mitigating hydrogen embrittlement of steels: A review of experimental, modelling and design progress from atomistic to continuum. *J. Mater. Sci.* **2018**, *53*, 6251–6290. [CrossRef]
37. Shuai, K.; Liu, H.; Li, M.; Yin, S.; Li, B.; Wang, B.; Liu, Q.; Jia, S. Hydrogen Embrittlement Sensitivity of X70 Welded Pipe Under a High-Pressure Pure Hydrogen Environment. *Materials* **2024**, *17*, 5818. [CrossRef] [PubMed]
38. *ASTM E1681-03:2020*; Standard Test Method for Determining Threshold Stress Intensity Factor for Environment-Assisted Cracking of Metallic Materials. ASTM International: West Conshohocken, PA, USA, 2021.
39. *BPVC.VIII.3*; BPVC Section VIII-Rules for Construction of Pressure Vessels Division 3-Alternative Rules for Construction of High Pressure Vessels. ASME USA: New York, NY, USA, 2025.
40. Campari, A.; Ustolin, F.; Alvaro, A.; Paltrinieri, N. A review on hydrogen embrittlement and risk-based inspection of hydrogen technologies. *Int. J. Hydrogen Energy* **2023**, *48*, 35316–35346. [CrossRef]

Disclaimer/Publisher's Note: The statements, opinions and data contained in all publications are solely those of the individual author(s) and contributor(s) and not of MDPI and/or the editor(s). MDPI and/or the editor(s) disclaim responsibility for any injury to people or property resulting from any ideas, methods, instructions or products referred to in the content.